Energy level spectroscopy of InSb quantum wells using quantum-well LED emission

T. G. Tenev and A. Palyi*
Department of Physics, University of Lancaster, Lancaster LA1 4YB, United Kingdom

B. I. Mirza
Department of Electrical and Electronic Engineering, Photonics Group, University of Bristol, Bristol BS8 1UB, United Kingdom

G. R. Nash†
QinetiQ, Malvern Technology Centre, Malvern WR14 3PS, United Kingdom
and Department of Electrical and Electronic Engineering, Photonics Group, University of Bristol, Bristol BS8 1UB, United Kingdom

M. Fearn, S. J. Smith, L. Buckle, M. T. Emeny, T. Ashley, and J. H. Jefferson
QinetiQ, Malvern Technology Centre, Malvern WR14 3PS, United Kingdom

C. J. Lambert
Department of Physics, University of Lancaster, Lancaster LA1 4YB, United Kingdom
(Received 11 July 2008; revised manuscript received 21 September 2008; published 2 February 2009)

We have investigated the low-temperature optical properties of InSb quantum-well (QW) light-emitting diodes, with different barrier compositions, as a function of well width. Three devices were studied: QW1 had a 20 nm undoped InSb quantum well with a barrier composition of $Al_{0.143}In_{0.857}Sb$, QW2 had a 40 nm undoped InSb well with a barrier composition of $Al_{0.077}In_{0.923}Sb$, and QW3 had a 100 nm undoped InSb well with a barrier composition of $Al_{0.025}In_{0.975}Sb$. For QW1, the signature of two transitions (CB1-HH1 and CB1-HH2) can be seen in the measured spectrum, whereas for QW2 and QW3 the signature of a large number of transitions is present in the measured spectra. In particular transitions to HH2 can be seen, the first time this has been observed in AlInSb/InSb heterostructures. To identify the transitions that contribute to the measured spectra, the spectra have been simulated using an eight-band $\mathbf{k}\cdot\mathbf{p}$ calculation of the band structure together with a first-order time-dependent perturbation method (Fermi golden rule) calculation of spectral emittance, taking into account broadening. In general there is good agreement between the measured and simulated spectra. For QW2 we attribute the main peak in the experimental spectrum to the CB2-HH1 transition, which has the highest overall contribution to the emission spectrum of QW2 compared with all the other interband transitions. This transition normally falls into the category of "forbidden transitions," and in order to understand this behavior we have investigated the momentum matrix elements, which determine the selection rules of the problem.

DOI: 10.1103/PhysRevB.79.085301 PACS number(s): 78.67.De, 78.60.Fi, 42.72.Ai

I. INTRODUCTION

There is growing interest in the development of $InSb/Al_xIn_{1-x}Sb$-based quantum wells (QWs) for uncooled, low power dissipation high-speed transistors,[1] for lasers,[2] and for devices exhibiting quantum effects such as quantized conductance,[3,4] where the low electron effective mass ($0.014m_e$) offers the prospect for elevated temperature operation due to enhanced quantum confinement.[4] The high electron g factor (~ -51) also makes $InSb/Al_xIn_{1-x}Sb$ QWs particularly attractive for quantum information applications.[5] Quantum confinement was first demonstrated in $InSb/Al_xIn_{1-x}Sb$ multiquantum-well (MQW) samples, grown on InSb substrates, using photoluminescence (PL) spectroscopy.[6] Recent developments in growth techniques have allowed high quality heterostructures to be grown on semi-insulating (SI) GaAs substrates, which is important for many device applications, and the optical properties of MQW structures grown on GaAs have been studied in absorption spectroscopy[7–9] and photoluminescence measurements.[10] However only one study of the optical properties of single InSb QWs, using photoluminescence, has so far been published,[11] although many novel devices could be perhaps realized using single InSb QWs. For example, such a well could be used to develop a high-frequency single-photon source emitting in the technologically important 3–5 μm wavelength region,[5] for example, at 3.9 μm, which could enable long-distance, free-space secure communication, via quantum cryptography, with low atmospheric scattering and absorption. In this proposed device, single electrons would be injected into the p-type region of a lateral InSb QW light-emitting diode (LED).[12] A greater understanding of the optical properties of single InSb QWs is therefore required before their unique characteristics, such as the high electron g factor can be fully exploited, and in this paper we analyze the low-temperature emission spectra of conventional vertical LEDs containing active regions consisting of InSb quantum wells of varying thicknesses.[13] Electroluminescence studies provide an exciting experimental platform that offers additional degrees of freedom, such as the ability to vary the net bias across the quantum wells that complement photoluminescence techniques. The measured emission spectra, which are compared to simulations carried out using an eight-band $\mathbf{k}\cdot\mathbf{p}$ model, exhibit a number

of features, including a large number of observed transitions, which reflect the unique properties of this material system.

II. THEORETICAL MODEL

A. Band-structure model

For the theoretical description of the QW-based LED we have chosen the z axis of the Cartesian coordinate system to lie along the growth direction of the device. The bulk band structure in the vicinity of the Γ point of InSb and its alloys is well described[14] by the semiempirical $\mathbf{k}\cdot\mathbf{p}$ method.[15,16] To find the energy spectrum and wave functions of electrons and holes localized in the QWs we employed the envelope function approximation (EFA) (Ref. 16–22) as the generalization of the $\mathbf{k}\cdot\mathbf{p}$ method for heterostructures. We took into account the heavy- and light-hole bands, with symmetry Γ_8^v, the spin-orbit split bands Γ_7^v, and the lowest conduction bands Γ_6^c, the ones used in an eight-band $\mathbf{k}\cdot\mathbf{p}$ description of bulk materials. For the band-edge Bloch functions $u_{j,\mathbf{k}=0}(r)$ we used the phase convention defined by Weiler.[23] Their explicit form can also be found in the Appendix of Ref. 24. Following Ram-Mohan *et al.*[24] we assumed that the basis set of zone-center Bloch functions $u_{j,\mathbf{k}=0}(r)$ is identical for the well (InSb) and barrier ($Al_xIn_{1-x}Sb$) materials.

Within the above framework the eigenfunctions of the single-particle Hamiltonian H are expressed as linear combinations of the band-edge Bloch functions

$$\Psi_{n,k}(r) = e^{ik_\parallel\cdot r_\parallel}\sum_j f_{nr_\parallel}^j(z)u_{j,k=0}(r), \tag{1}$$

where $k_\parallel=(k_x,k_y,0)$ and $r_\parallel=(r_x,r_y,0)$ and the expansion coefficients, the envelope functions $f_{nk_{\parallel}}^j(z)$, are supposed to vary slowly over the lattice unit cells. The eigenvalue problem $H\Psi_{n,k_\parallel}(r)=E_n(k_\parallel)\Psi_{n,k_\parallel}(r)$ reduces to a set of eight coupled differential equations for the envelope functions $f_{nk_\parallel}^{j'}(z)$

$$\sum_{j'} H_{jj'}(k_x,k_y,-i\,\partial/\partial z)f_{nk_\parallel}^{j'}(z) = E_n(k_\parallel)f_{nk_\parallel}^{j'}(z). \tag{2}$$

In the chosen representation[23] the matrix elements $H_{jj'}$ of the Hamiltonian are identical to the one given in Table III of Ref. 24. In the absence of magnetic field the Hamiltonian matrix elements $H_{jj'}$ are parametrized by the interband matrix element P [14]; the Kane parameter F;[14] the modified-Luttinger[24–27] parameters γ_1, γ_2, and γ_3; and the band gap E_g and spin-orbit split-off energies Δ relative to the Γ_8^v valence-band edge.

We used the axial approximation by setting the modified Luttinger parameters γ_2 and γ_3 equal to each other and equal to $\gamma=(2\gamma_2+3\gamma_3)/5$.[24] The axial approximation neglects the anisotropy in the dispersion relations $E_n(k_\parallel)$. Furthermore we neglected the material dependence of the parameters P, F, γ_1, γ_2, and γ_3. For the interband matrix element P we used the value for InSb reported by Auvergne *et al.*[28] We took the recommended values from Table IX of Ref. 14 for the other band-structure parameters of InSb.

The temperature dependencies of the InSb and AlSb band gaps E_g were taken into account through the empirical Varshni law[14] using the values for the Varshni parameters α and β given in Ref. 14. The band gap and spin-orbit splitting dependence of the $Al_xIn_{1-x}Sb$ alloy of composition fraction x were accounted for using the following quadratic interpolation formula:[14,29]

$$T(Al_xIn_{1-x}Sb) = xT(AlSb) + (1-x)T(InSb) - x(1-x)C_T, \tag{3}$$

where T stands for either E_g or Δ. We have used the values recommended by Vurgaftman *et al.*[14] for the bowing parameters C_T. Through Eq. (3) we have also accounted for the temperature dependence of the alloy band gap by using temperature-dependent values for the InSb and AlSb band gaps.

Strain due to the lattice constant mismatch between the $Al_xIn_{1-x}Sb$ alloy and InSb was included in our model through its effect on the InSb band gap. The lattice constant of $Al_xIn_{1-x}Sb$ was determined by Vegard's law[30] with temperature-dependent values of InSb and AlSb lattice constants taken from Ref. 14. The compressive biaxial strain lifts the light- and heavy-hole degeneracies at the Γ point.[32] Using the methods described by Dai *et al.*[7] and Kasturiarachchi *et al.*[31] and material parameters for InSb and AlSb as recommended by Vurgaftman *et al.*,[14] we have calculated the strained band gaps between the conduction and heavy- and light-hole bands, respectively, and used them as input parameters in our simulations. For the conduction-band offset ratio Q_c we assumed the value $Q_c=0.62$.[31]

We treated the model given by Eq. (2) numerically, assuming that the envelope functions vanish at the surface of the sample and deep inside the substrate. The solutions of the eigenvalue problem were found by expanding the envelope functions in a Fourier series and expressing the matrix elements $H_{jj'}$ of the EFA Hamiltonian in the Fourier basis. The resulting matrix was diagonalized numerically using standard LAPACK routines.

B. Luminescence model

The microscopic mechanism underlying electroluminescence in semiconductor quantum wells is the spontaneous emission of light due to electron-hole recombination. The spontaneous emission is purely a quantum mechanical process which requires a quantum description of the electromagnetic (EM) field. We have used the standard quantization in a finite volume procedure[33] for the EM vector-potential operator $\hat{A}(\vec{r},t)$ and worked in SI units. In this paradigm a classical EM wave characterized by wave vector $\vec{q}$, polarization vector $\vec{\varepsilon}_\lambda \perp \vec{q}$, and angular frequency $\omega_q=c|\vec{q}|$ is viewed as a collection of photons in single-particle modes $|\vec{q}\lambda\rangle$ characterized by two quantum numbers $\vec{q}$ and λ. The number of possible photon modes per unit energy describing photons propagating in solid angle $d\Omega$ with definite polarization is given by the photon density of states $\rho(\hbar\omega)=V\omega^2n^3/\hbar(2\pi c)^3$,[33,34] where n is the refractive index of the medium and V is the quantization volume.

The number of λ polarized photons emitted per unit energy interval per second in a solid angle $d\Omega$ due to electron-

hole recombination in the volume of a quantum well is given by the expression

$$N_{\hat{q}\lambda}(\hbar\omega) = \sum_{n,m} \sum_{\vec{k}_\parallel} W_{nm\vec{k}_\parallel,\vec{q}\lambda} \rho(\hbar\omega) f[E_n(\vec{k}_\parallel)]\{1 - f[E_m(\vec{k}_\parallel)]\}, \tag{4}$$

where the summation is over all pairs of electron-hole states, $f[E_n(\vec{k}_\parallel)]$ is the statistical probability that the conduction-band state $|n\vec{k}_\parallel\rangle$ is occupied, and $1-f[E_m(\vec{k}_\parallel)]$ is the probability that the valence band state $|m\vec{k}_\parallel\rangle$ is empty. We assume that the relaxation time of electrons and holes injected into the quantum well is much shorter than the radiative recombination time. Therefore, on the timescale of electron-hole recombination, the hole and electron gases behave effectively as being in thermodynamic equilibrium characterized by some effective temperature T_e, which in general is different and higher than the temperature of the host crystal lattice T_c. In this approximation the statistical distribution function $f(E)$ takes the simplified form of the Fermi-Dirac function $f(E) = 1/\{1+\exp[(E-\mu)/k_B T_e]\}$, where k_B is the Boltzmann constant and μ is the chemical potential of either electrons or holes. The probability for a transition from conduction-band state $|n\vec{k}_\parallel\rangle$ to valence-band state $|m\vec{k}_\parallel\rangle$ per unit time $W_{nm\vec{k}_\parallel,\vec{q}\lambda}$ is calculated within the first-order, time-dependent perturbation method (Fermi golden rule),[35] using the following dipole approximation:[33,36]

$$W_{nm\vec{k}_\parallel,\vec{q}\lambda} = \frac{2\pi}{\hbar}\delta[\hbar\omega_{nm}(\vec{k}_\parallel) - \hbar\omega]\frac{\hbar}{2\varepsilon\omega V}\frac{e^2}{m^2 n^2}|\langle m\vec{k}_\parallel|\vec{p}\,.\,\vec{\varepsilon}_\lambda|n\vec{k}_\parallel\rangle|^2, \tag{5}$$

where m is the free-electron mass, ε is the dielectric constant of the medium, e is the electron charge, n is the refractive index of the medium, $\vec{\varepsilon}_\lambda$ is the polarization vector of the EM field, and $\omega_{nm}(\vec{k}_\parallel)$ is the Bohr frequency of the transition between states $|n\vec{k}_\parallel\rangle$ and $|m\vec{k}_\parallel\rangle$ determined by the equation $\hbar\omega_{nm}(\vec{k}_\parallel) = E_n(\vec{k}_\parallel) - E_m(\vec{k}_\parallel)$. The conservation of energy in the emission process is enforced by the Dirac delta function in Eq. (5) which also ensures that only resonant transitions fulfilling the condition $\omega = \omega_{nm}(\vec{k}_\parallel)$ contribute to the emitted radiation. Information about the effects of the electron energy subband structure in the quantum well is contained in the momentum matrix element $\langle m\vec{k}_\parallel|\vec{p}|n\vec{k}_\parallel\rangle$ and the electron and hole subband dispersion relations $E_n(\vec{k}_\parallel)$ and $E_m(\vec{k}_\parallel)$.

Photons with the same frequency resulting from spontaneous emission between different states have uncorrelated propagation directions and polarizations. The resulting EM field is represented by the total number of emitted photons $N(\hbar\omega)$ with angular frequency ω which is obtained by summing $N_{\hat{q}\lambda}(\hbar\omega)$ over the two linearly independent polarization modes $\lambda = \pm 1$ and integrating over all propagation directions $N(\hbar\omega) = \int_\Omega d\Omega \Sigma_\lambda N_{\hat{q}\lambda}(\hbar\omega)$, where Ω is the unit sphere. The total energy carried by the emitted radiation per unit energy interval per unit time is given by the product of $N(\hbar\omega)$ and the energy carried by each photon $\hbar\omega$, $P(\hbar\omega) = N(\hbar\omega)\hbar\omega$. The experimentally observable spectral emittance is the EM energy per unit time and unit energy interval passing through unit surface area at distance r, $I(\hbar\omega) = P(\hbar\omega)/4\pi r^2$ $(WJ^{-1}m^{-2})$.

In the derivation of Eq. (5) we have assumed that the conduction- and valence-band energy levels are well defined. In practice there are a number of environmental factors which lead to deviation from the ideal delta peak shape of the transition introducing broadening into the line shape. The underlying mechanisms are usually classified into the two groups of homogeneous and inhomogeneous broadening. The natural linewidth and electron-phonon scattering are usual sources of homogeneous broadening. As is usually accepted[37–39] we modeled their effect on the emission line shape by the substitution of the Lorentzian function $L(\hbar\omega, \hbar\omega_{nm}(\vec{k}_\parallel); \Gamma_H)$ instead of the Dirac delta in Eq. (5) where the homogeneous linewidth Γ_H is the full width at half maximum (FWHM) of the Lorentzian. The combined effect of the individual homogeneous mechanisms is modeled by a convolution of Lorentzians, which is again Lorentzian with FWHM $\Gamma_H = \Gamma'_H + \Gamma''_H + \cdots$, where the primed FWHM are the contributions from the individual mechanisms.

Possible sources of inhomogeneous broadening are well width fluctuations across an individual well or well-to-well width fluctuations arising during QW growth. They lead to statistical distribution of the Bohr frequencies of the transition $\omega_{nm}(\vec{k}_\parallel)$ around the values for an ideal well. We have assumed that the transition energies E associated with the Bohr frequencies are normally distributed around the ideal value $\hbar\omega_{nm}(\vec{k}_\parallel)$ for the transition $|n\vec{k}_\parallel\rangle \rightarrow |m\vec{k}_\parallel\rangle$ with FWHM of the Gaussian Γ_I. Contributions of the individual mechanisms to the overall inhomogeneous broadening is given by the expression[40] $\Gamma_I^2 = \Gamma_I'^2 + \Gamma_I''^2 + \cdots$.

The combined effects of the two types of broadening are taken into account by the Voight function which is a convolution of the Lorentzian and Gaussian functions described above and is explicitly given by

$$U[\hbar\omega, \hbar\omega_{nm}(\vec{k}_\parallel); \Gamma_I, \Gamma_H] = \frac{A}{\pi^{3/2}\sqrt{2}\Gamma_I}\int_0^\infty dE \frac{(\Gamma_H/2)}{(\hbar\omega - E)^2 + (\Gamma_H/2)^2} \times \exp\left\{-\frac{[E - \hbar\omega_{nm}(\vec{k}_\parallel)]^2}{2\Gamma_I^2}\right\}, \tag{6}$$

where the lower limit of the integration is restricted to zero because of the interpretation of the integration variable as a transition energy. This line shape has been used for the determination of the linewidth of intersubband transitions[37] in the InGaAs/AlGaAs system and for the description of the line shape in the vicinity of the exciton absorption lines in GaAs multiple quantum wells.[41] The normalization constant A arises from the conservation of energy principle enforced by the integral of the Voight function over all possible transition energies $\hbar\int d\omega_{nm} U(\hbar\omega, \hbar\omega_{nm}(\vec{k}_\parallel); \Gamma_I, \Gamma_H) = 1$. For the sake of computational efficiency we have used the approximation to the Voight function developed in Ref. 40.

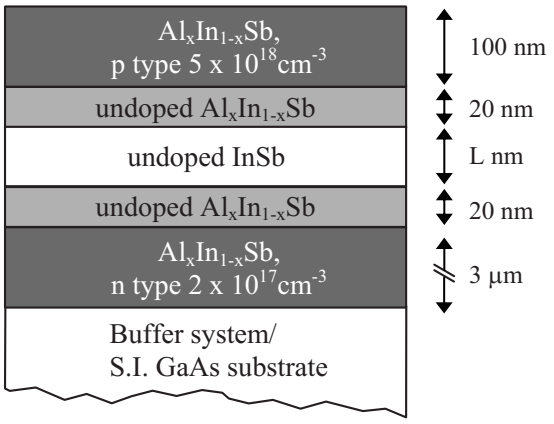

FIG. 1. Schematic cross section showing the structure of the QW LEDs. L is the quantum-well thickness.

The final explicit form of the spectral emittance which we have used to interpret the experimental data is thus given as follows:

$$I(\hbar\omega) = \sum_{n,m} \sum_{\vec{k}_\parallel} \frac{e^2}{4\pi^2 \varepsilon r^2} \frac{\omega^2 n}{3m^2 c^3} U[\hbar\omega, \hbar\omega_{nm}(\vec{k}_\parallel); \Gamma_I, \Gamma_H] \times |\langle m\vec{k}_\parallel | \hat{\vec{p}} | n\vec{k}_\parallel \rangle|^2 f[E_n(\vec{k}_\parallel)]\{1 - f[E_m(\vec{k}_\parallel)]\}, \quad (7)$$

III. EXPERIMENTAL METHOD

The samples studied were grown by molecular-beam epitaxy at QinetiQ Malvern on SI GaAs substrates.[1] A schematic diagram of the QW LED structure is shown in Fig. 1. The InSb QWs were grown on top of a 3-μm-thick $Al_xIn_{1-x}Sb$ barrier and were capped with a 120-nm-thick layer of $Al_xIn_{1-x}Sb$. Tellurium and beryllium were used to dope the layers n type and p type to nominal levels of 2×10^{17} and 5×10^{18} cm^{-3}, respectively. Three QW LED structures were investigated: QW1 had a 20 nm undoped InSb quantum well with a barrier composition of $x=0.143$; QW2 had a 40 nm undoped InSb well with a barrier composition of $x=0.077$; and QW3 had a 100 nm undoped InSb well with a barrier composition of $x=0.025$. The composition of the barrier layers was determined by x-ray diffraction measurements. Devices consisted of 16 elements connected in series yielding a total emitting area of 1 mm^2. More details concerning device structure, growth, and doping can be found in Ref. 13 (and references therein). The devices were mounted on ceramic packages in a closed cycle cryostat, with optical access through a CaF_2 window. Emitted light from the devices was collimated using a CaF_2 lens and directed to a SPEX 270 M grating spectrometer (with a 5 μm blazed grating). Peak injection currents used were 2 mA for QW1 and 20 mA for QW2 and QW3. Measurements were carried out at either 15 or 25 K.

IV. RESULTS AND DISCUSSION

A. Overview

The interpretation of the experimental results in the present study is an example of the reverse problem in theoretical physics. In its most general formulation one has to understand and describe a set of interrelated physical effects and mechanisms determining the experimental results based mostly on the experimental observations. We solved the problem for the spontaneous emission from QW1, QW2, and QW3 by the method of line-shape fitting employing the theoretical model described in Sec. II which contains five fitting parameters: the effective temperature T_e, the injected carrier density in the well n, the homogeneous broadening Γ_H, the inhomogeneous broadening Γ_I, and the net bias across the quantum well V_{net}.

We have assumed that the electron and hole gases can be characterized by the same effective temperature T_e.[39] The condition for charge neutrality in the quantum well as a whole requires that the injected carrier density for electrons is equal to that of holes $n_e=n_h=n$. The net bias across the well is the difference between the built-in potential of the p-i-n junction and the voltage drop across it due to the externally applied voltage. Estimation of this voltage drop is unreliable due to the contact resistance present in the device architecture. The contact resistance depends on the growth conditions which may vary from sample to sample. We have therefore treated the net bias across the quantum well as a fitting parameter. We have minimized the weighted chi-squared $\chi^2(T_e, n, \Gamma_H, \Gamma_I, V_{\text{net}})$ function in the five-dimensional parameter space using the global nonlinear minimization algorithm of simulated annealing (SA) (Refs. 42 and 43) subject to constraints in the parameter space. For selected cases we have compared the results of the χ^2 minimization by the SA with the more accurate, but computationally much more intensive, differential evolution algorithm.[44] The results were in satisfactory agreement, giving us confidence in the parameter estimates obtained by SA.

The best fit between experiment measurements and theoretical calculations and the values of the five fitting parameters have been determined as the values of $T_e, n, \Gamma_H, \Gamma_I, V_{\text{net}}$ which give the minimum value of χ^2, according to the general theory of optimization. We have not supposed any particular values for the fitting parameters $T_e, n, \Gamma_H, \Gamma_I, V_{\text{net}}$, rather their values have been calculated by the SA (Refs. 42 and 43) minimization algorithm. Furthermore the comparison between the experimental and theoretical line shapes presented in Figs. 3(a), 4(a), and 5(a) is to serve only as a visual confirmation for the quality of the fit and not as the criterion for it. The criteria for the best fit is the minimum of the *maximum-likelihood estimator* $\chi^2(T_e, n, \Gamma_H, \Gamma_I, V_{\text{net}})$.[45] The contribution of different types of transitions to the observed spectrum has not been determined on the basis of simple identification of sharp features in the experimental spectrum but rather upon the examination of the simulated threshold energies for the transitions [designated with arrows in Figs. 3(a), 4(a), and 5(a)], the optical transition matrix elements as the generalization of the "optical selection rules," and ultimately from the simulated emission from a particular transition for the estimated values of the fitting parameters $T_e, n, \Gamma_H, \Gamma_I, V_{\text{net}}$.

B. Basic band-structure effects

1. Zero-bias simulations

In order to gain a better understanding of the mechanisms of electroluminescence in the studied low-dimensional het-

TABLE I. Best-fit parameters for the three quantum wells.

Parameters	QW1	QW2	QW3
V_{net} (kV cm^{-1})	12	14	2.3
T_e (K)	45	105	129
n (10^{10} cm^{-2})	10	6.77	24
Γ_I (meV)	4	5.7	0.35
Γ_H (meV)	0.5	0.7	0.2

erostructures, we have performed reference simulations for the energy subband structure at zero net bias $V_{net}=0$. These were compared with the band-structure simulations, which were performed using the value for the net bias V_{net} obtained from the best-fit parameters for the three QWs as presented in Table I. This has allowed us to separate the influence of finite net bias across the QWs on their energy subband structures and the effects resulting from that. Results from the $V_{net}=0$ simulations for conduction-band, heavy-hole band, and light-hole band edges as functions of the growth direction z, together with the bottoms of the conduction and hole subbands for the three quantum wells, are plotted in Figs. 2(a)–2(c) for QW1, QW2, and QW3, respectively. As mentioned in Sec. II A, the compressive biaxial strain lifts the light- and heavy-hole degeneracies at the Γ point. Comparison of the three figures shows an increase in the number of confined subbands with increasing well thickness in line with the general predictions of size quantization. These subband structure effects imply that we can expect more transitions to contribute to the overall emission spectrum for wider wells eventually leading to more well-pronounced peaks in the emission spectrum with increased well width. An additional effect of the size quantization is the decrease in the electron and hole energy upshifts for increasing well width, which is very well pronounced for the electron band structure shown in Figs. 2(a)–2(c). It is still valid for the hole band structure, but is not so well resolved due to the higher effective mass of the hole subbands. The reduction in the energy upshifts means that the effective band gap E_g^{eff}, defined as the energy difference between the bottom of the first electron and hole subbands $E_g^{\text{eff}}=E_1^e(0)-E_1^h(0)$, is inversely proportional to the well width. As the onset of the spontaneous emission spectrum is determined by the effective band gap E_g^{eff}, in the absence of exciton transitions and broadening, the performed simulations predict a slight redshift in energy for the onset of emission with increasing well width. Taking as a reference the effective band gap E_g^{eff} of QW1 (20 nm wide), our simu-

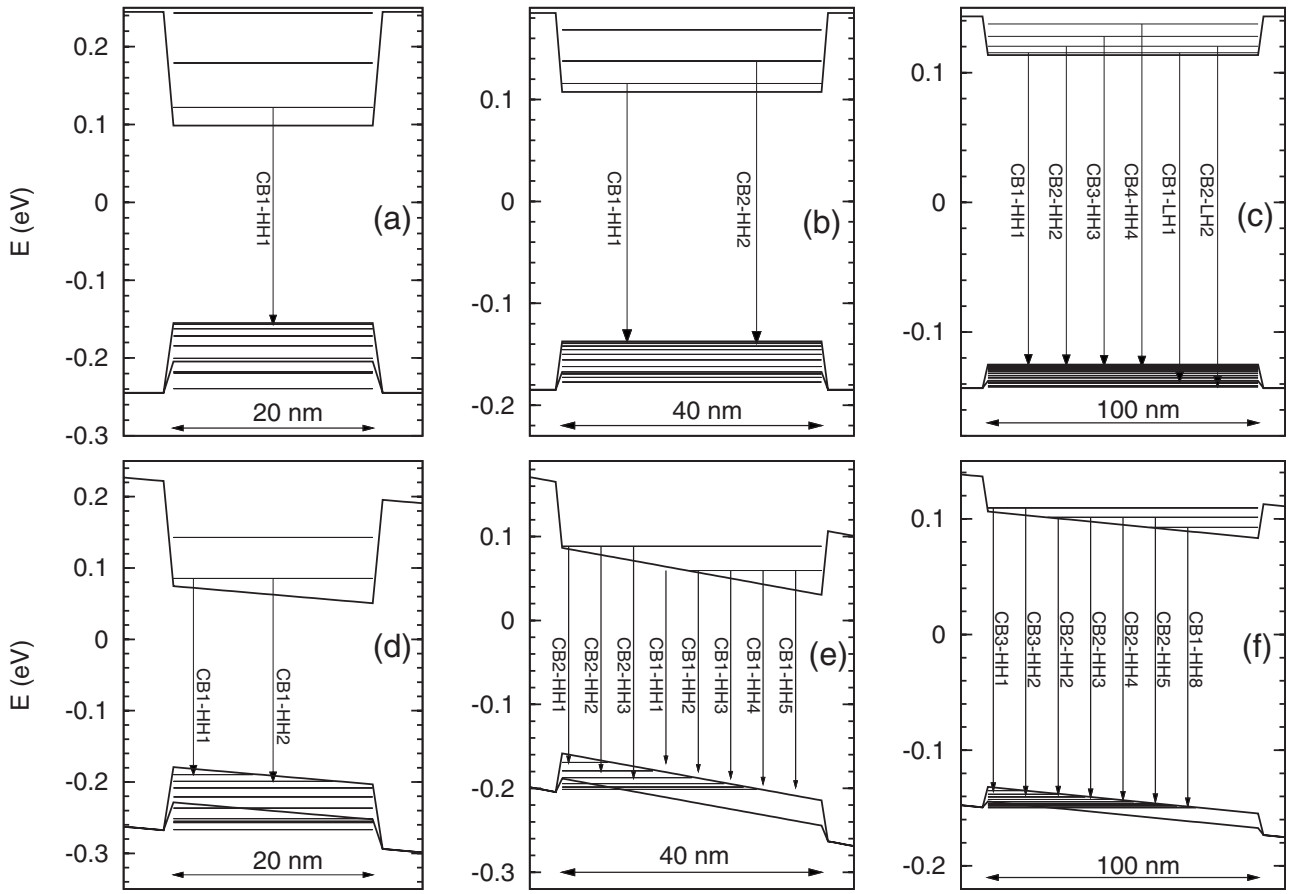

FIG. 2. Real-space energy diagrams of conduction-band, heavy-hole band, and light-hole band edges as functions of transverse direction z for quantum wells of sizes 20 (QW1), 40 (QW2), and 100 (QW3) nm, under zero and finite net biases across the wells. The band edges are represented by thick lines; in particular, the thick line in the hole subband represents the light-hole band edge. The bottoms of the conduction and hole subbands resulting from the size quantization in the QWs are shown as horizontal lines in the wells. The threshold energies of the transitions are designated with arrows and associated labels.

lations predict a 21.6 meV decrease in E_g^{eff} for QW2 (40 nm wide) and a 28.5 meV decrease in E_g^{eff} for QW3 (100 nm wide).

The variation in the aluminum (Al) concentration x in the barrier material $Al_xIn_{1-x}Sb$ of the three QW structures influences the energy band structure in two ways. First, according to the combination of Eq. (3) with the value of the bowing parameter C_T,[14] the band gap of the barrier material $Al_xIn_{1-x}Sb$ is directly proportional to the Al concentration x. The Al concentration in the experimental samples increases with decreasing well width having the largest value for QW1 (20 nm wide). We have estimated that the barrier band gap for QW1 is $E_g(Al_{0.143}In_{0.857}Sb)=489.4$ meV, while the barrier band gap for QW3 is $E_g(Al_{0.025}In_{0.975}Sb)=286.6$ meV. In addition to the modification of the barrier band gap the presence of Al in the barrier changes its lattice constant leading to mismatch between the lattice constants of the well and barrier materials. The resulting compressive biaxial strain modifies the bulk band edges in the QWs lifting the HH-LH degeneracy at the Γ point as indicated in Fig. 2 and changes the fundamental energy band gap, which in the present case is CB-HH. The fundamental band gap therefore increases with increasing Al concentration, thus having an opposite effect on the depths of the electron and hole potential wells than the increase in the barrier band gap. Using the method[7,14,30,31] described in Sec. II, we have calculated that the fundamental energy gap for QW1 is $E_g^{\text{well}}=253.8$ meV, while that for QW2 is $E_g^{\text{well}}=238.7$ meV. This energy difference caused by the variation in Al concentration is of the order of 20 meV or an order of magnitude smaller than the 200 meV energy difference due to the change in the barrier band gap. Therefore we conclude that the dominant effect of the Al concentration on the electron and hole potential well depths is due to the modification of the barrier band gap $E_g(Al_xIn_{1-x}Sb)$. For the studied devices the resulting decrease in the potential well depths with increasing QW width, which can be clearly seen by comparing Figs. 2(a)–2(c), competes against the size quantization effects with regard to the number of confined electron and hole subbands. Inspection of Figs. 2(a)–2(c) shows that the two competing factors nearly balance each other for the case of electron subbands, although the size quantization prevails with four confined subbands in QW3 against two in QW1. In the case of hole subbands the size quantization is the prevailing effect leading to a considerable amount of confined hole subbands for QW3 as can be easily verified by inspecting Figs. 2(a)–2(c). This leads to a considerable effect on the emission spectrum by increasing the number of transitions which contribute.

2. Finite bias simulations

The results for the energy subband structure and electron and hole potential wells from simulations performed with the best-fit value of the net bias V_{net} are shown in Figs. 2(d)–2(f) for QW1, QW2, and QW3, respectively. The net bias V_{net} modifies both the energy subband structure and the electron $|n\vec{k}_{\|}\rangle$ and hole states $|m\vec{k}_{\|}\rangle$, through which it has influence on the emission spectrum of the QWs. The changes induced by V_{net} on the electron $E_n^e(\vec{k}_{\|})$ and hole spectra $E_m^e(\vec{k}_{\|})$ through the quantum confined Stark effect (QCSE) (Ref 46) lead to a decrease in E_g^{eff} with increasing net bias. For the three QWs studied the decrease in E_g^{eff} is of the order of 10 meV over the relevant bias range. The decrease in E_g^{eff} is reflected as a redshift in energy to the onset of the spontaneous emission spectrum. In general the increase in the net bias does not necessary lead to a decrease in the threshold transition energies $E_{nm}=E_n(0)-E_m(0)$ for every pair of possible transitions. It is possible that some threshold transition energies E_{nm} actually increase, but the detection of these in the emission spectrum can be difficult due to a background of other subband transitions $E_{nm}(\vec{k}_{\|})=E_n(\vec{k}_{\|})-E_m(\vec{k}_{\|})$ for higher values of the two-dimensional (2D) crystal momentum wave vector $\vec{k}_{\|}$. In addition to the QCSE the bias V_{net} across the well leads to lifting of the spin degeneracy away from the Γ point in the absence of external magnetic field, due to spin-orbit coupling effects,[16] but our simulations showed that these effects are irrelevant for the unpolarized emission spectrum. This is consistent with the fact that only energy splittings at the Γ point can eventually manifest themselves in the unpolarized luminescence spectrum.

The influence of the net bias on the electroluminescence spectrum through the modification of the electron $|n\vec{k}_{\|}\rangle$ and hole $|m\vec{k}_{\|}\rangle$ states leads not only to quantitative changes as in the case of QSCE but also to qualitative modification of the properties of the momentum matrix elements $\langle m\vec{k}_{\|}|\vec{p}|n\vec{k}_{\|}\rangle$ which may be manifested as observable features in the spontaneous emission spectrum. Furthermore the presence of a net bias across the quantum wells breaks the inversion symmetry of the heterostructure potential with respect to the center of the devices, referred to as structure inversion asymmetry (SIA).

Standard selection rules, as described in Ref. 36, are based on a model for the electron and hole states which does not take into account band mixing. Under this approximation, for symmetrical quantum wells, the selection rule on the subband quantum numbers n,m, which is obtained from the overlap of the envelope functions, is determined from the global property that the envelope functions have definite parity with respect to the center of the well. This restricts the set of allowed transitions to those satisfying the condition $n+m=$even.[36] In the GaAs/AlGaAs material system the transitions $n-m=0$ are much stronger that the remainder of the allowed transitions.[36] This has limited studies of the $InSb/Al_xIn_{1-x}Sb$ system only to such transitions.[7,31] Often transitions satisfying the conditions $n+m=$even, or just the stronger condition $n-m=0$, are referred to as "allowed transitions," while the rest are referred to as "forbidden transitions." Transitions of this type, relevant for the studied QWs, are shown in Fig. 2(a)–2(c). In the case of SIA the transitions for which $n+m$ is odd are also allowed, although the asymmetry must be very strong.[36] In the eight-band model for electron and hole states, Eq. (1), due to the mixing of the electron and the three different hole states of both even and odd parities at $\vec{k}_{\|}$, points away from the Γ point and vertical transitions between all pairs of subband states become possible[47–49] even in symmetric quantum wells. However, the question of which are the strongest transitions, which transitions have dominant contribution to the observed spec-

trum, and why exactly these transitions contribute to the measured spectra in the presence of net bias across the QWs need to be addressed. We have indicated with arrows and associated labels the relevant transitions, determined to contribute to the observed spectrum in Figs. 2(d)–2(f) for QW1, QW2, and QW3, respectively.

C. QW1 (20 nm)

To gain insight into the problems described above we have first performed line-shape fitting of the experimentally measured spectrum using the model described in Sec. II, in particular using the expression for spectral emittance given by Eq. (7). The fitting parameter values, as determined by the minimum of the weighted χ^2 function found by the simulated annealing algorithm,[42,43] are given in Table I. Using these parameter estimates we have simulated the separate contributions of every transition to the overall spectrum by examining the spectral emittance due to every term in the sum over the different transitions in Eq. (7). The results from this procedure are presented in Figs. 3–5 for QW1, QW2, and QW3, respectively. In the upper plots we have shown the experimentally measured spectrum as dashed lines, with the calculated best fit represented as solid lines. Minima in all the measured spectra seen at around 292 meV are due to CO_2 absorption, which we have attempted to account for in the interpretation of the experimental results by using weighting factors in the calculation of the χ^2 function for the energy range of 284–300 meV.

For QW1 [Fig. 3(a)] there is some discrepancy between the measured and best fit at the onset of the spectrum in the energy range of 256–280 meV. We propose that this is due to exciton transitions, based on the knowledge that the exciton binding energies in general increase with decreasing well size,[36] that the optical properties of GaAs/AlGaAs QWs are dominated by the exciton transitions,[36] and the size of the exciton binding energy in bulk InSb.[50] The shoulder visible at ~265 meV in the data taken at 2 mA becomes much larger (in comparison to the peak at higher currents) as the current is decreased. The energy separation between this shoulder and the main peak is consistent with recent observations of bound excitons in the same material system.[51] Coupled with the small change in the energy at which this shoulder occurs with decreasing current, these results suggest that this feature is due to a bound exciton. Extensive treatment of the exciton states within the eight-band EFA Hamiltonian and exciton optical transitions for the InSb/AlInSb system is in development.

The simulated contributions from the relevant transitions $n \rightarrow m$ to the total simulated signal for QW1 using the best-fit parameters from Table I are shown in Fig. 3(b) together with the total simulated signal. Clearly the transitions from the first conduction subband (CB1) to the first (HH1) and second (HH2) hole subbands are the ones which form the shape of the full signal. The peak of the full signal is associated with the CB1-HH1 transition, while the CB1-HH2 transition contributes mainly to the higher-energy part of the full signal where its contribution is masked by the CO_2 absorption. The two hole subbands have heavy-hole character at the Γ point,

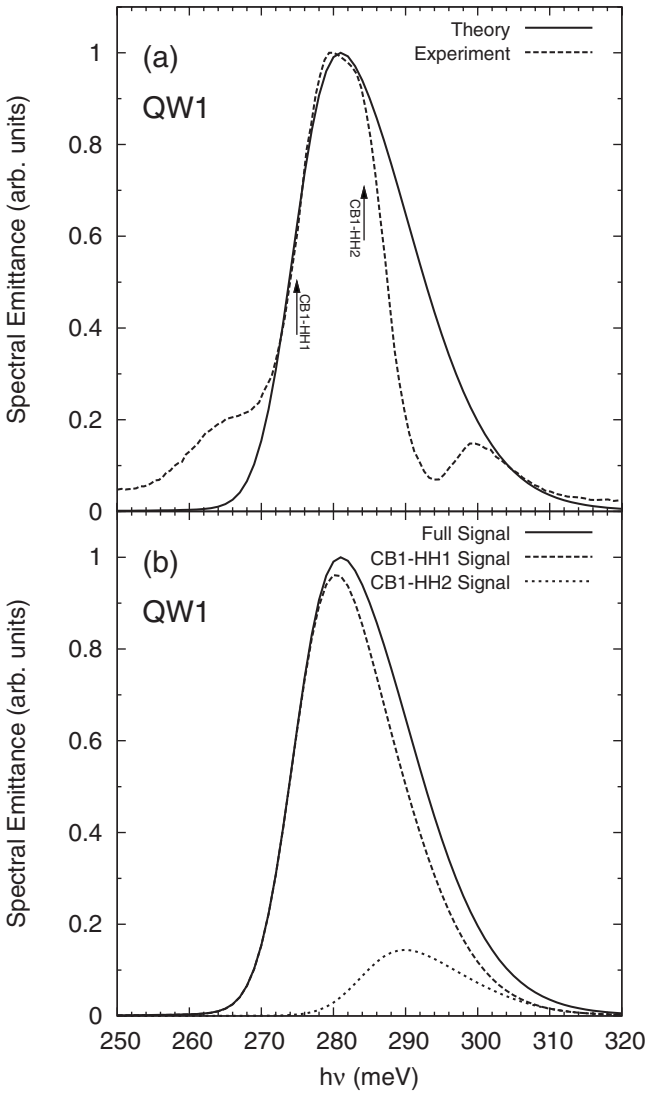

FIG. 3. Measured (at 15 K) and simulated spectral emittance from LED sample QW1 (20 nm). The upper subplot shows the experimentally measured and theoretically simulated spectral emittance for QW1. The threshold energies of the relevant interband transitions are designated with arrows and associated labels. The lower subplot shows the simulated spectral emittance due to spontaneous emission from the well together with the signal due to the relevant interband transitions.

although away from it, $\vec{k}_{\|} \neq 0$, the hole subband states may have strong admixture from light-hole zone-center states and less from conduction-band and split-off subband contributions. Despite this we will use the traditional labeling of the hole subbands by the dominant zone-center Bloch states $u_{j,\mathbf{k}=0}(r)$ in the linear combination [Eq. (1)] at the Γ point. The observation that mainly transitions to heavy-hole states contribute to the observed spectrum applies also to QW2 and QW3. This can be explained by the heavy-hole light-hole splitting at the Γ point caused by the compressive biaxial strain due to Al in the barrier. The effect is clearly illustrated in Fig. 2, where one can see that the HH-LH splitting is larger than half the depth of the hole potential well. In addition we see clearly that the ratio of the HH-LH splitting to

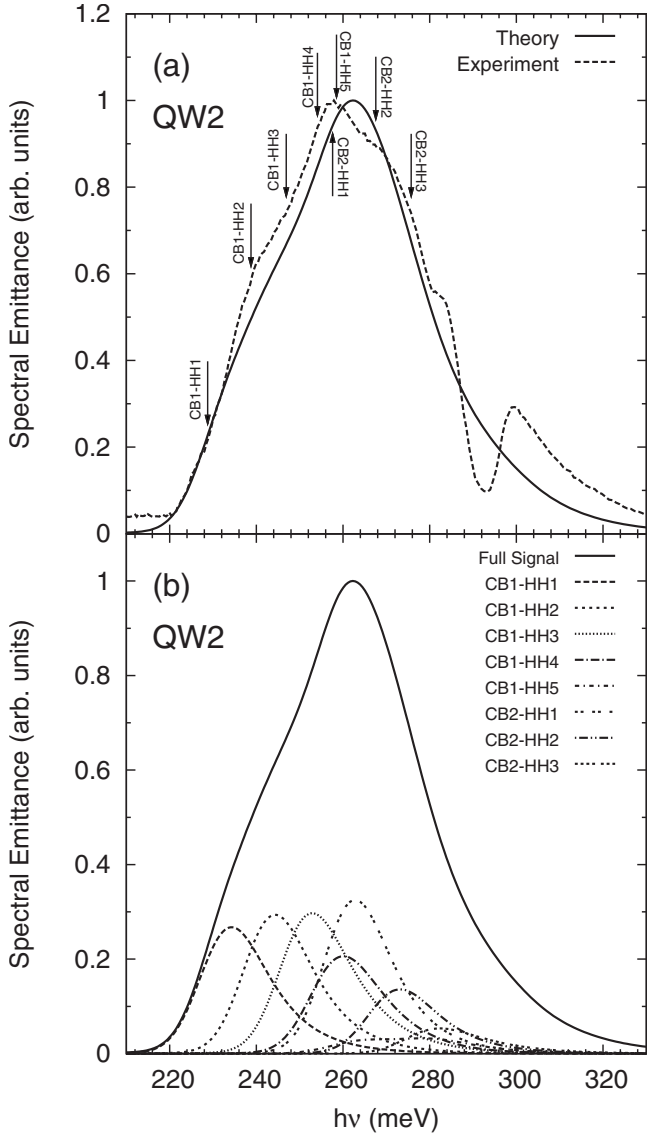

FIG. 4. Measured (at 15 K) and simulated spectral emittance from LED sample QW2 (40 nm). The upper figure shows the experimentally measured and theoretically simulated spectral emittance for QW2. The threshold energies of the relevant interband transitions are designated with arrows and associated labels. The lower figure shows the simulated spectral emittance due to spontaneous emission from the well together with the signal due to the relevant interband transitions.

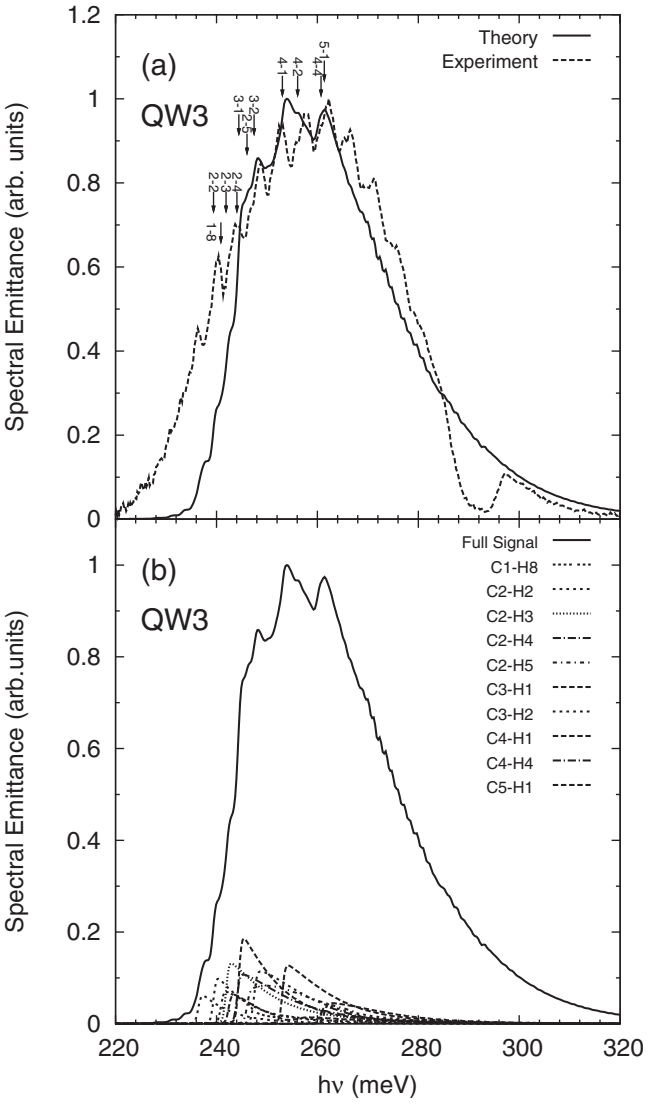

FIG. 5. Measured (at 25 K) and simulated spectral emittance from LED sample QW3 (100 nm). The upper figure shows the experimentally measured and theoretically simulated spectral emittance for QW3. The threshold energies of the relevant interband transitions are designated with arrows and associated labels. The lower figure shows the simulated spectral emittance due to spontaneous emission from the well together with the signal due to the relevant interband transitions.

the depth of the hole potential well increases with well width. Thus the opportunity for observation of CB-LH transitions decreases with increasing well width.

To the best of our knowledge this is the first report of the CB1-HH2 transition in InSb/AlInSb quantum-well heterostructures. Although this transition is not seen as a separate peak in the measured spectrum, one can observe a small shoulder in the high-energy part of the measured spectrum peak structure which we attribute to the CB1-HH2 transition. This transition is not from the set of $n+m=$even transitions, which are the allowed transitions in a single band model and zero net bias. The significance of this transition for emission from QW1 can be attributed to the nonzero net bias across the well, which is realistically an unavoidable feature in *p-i-n* diodes, and also to conduction and hole band nonparabolicity, which stresses the need for the use of the 8 band EFA method for an improved description of quantum-well subband structure and the resulting optical properties.

D. Broadening effects

By comparing simulations performed without account for the broadening mechanisms with simulations performed over a range of values for both types of broadening, we have concluded that the main reason that the CB1-HH2 transition is not better resolved in the measured spectrum is due to the combined effects of homogeneous and inhomogeneous

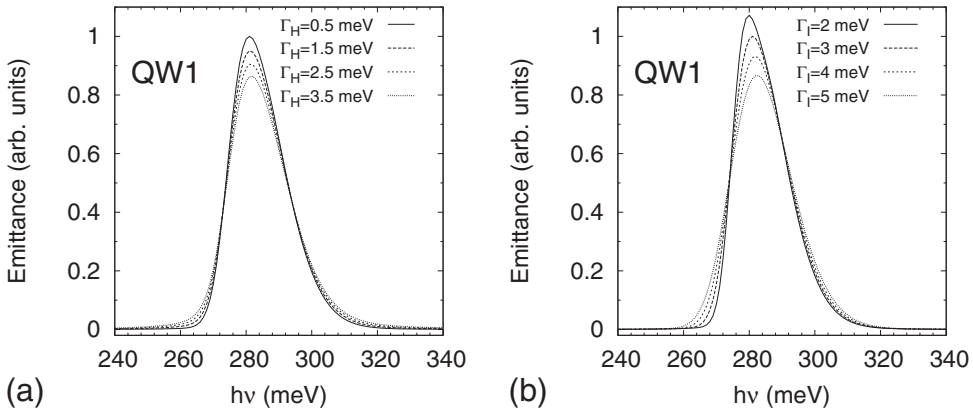

FIG. 6. Simulated emission spectra for QW1 (at 15 K) as a function of homogeneous and inhomogeneous broadenings. Spectral emittance line shape as a function of homogeneous and inhomogeneous broadenings for the 20 nm well simulated for effective temperature and injected carrier density. The peak height of the data resulting from simulation with homogenous broadening and inhomogeneous broadening has been normalized, and the results of the other simulations have been scaled with respect to it.

broadening. This can be understood by examining the effect of the broadening function $U(\hbar\omega,\hbar\omega_{nm}(\vec{k}_\parallel);\Gamma_I,\Gamma_H)$ in the expression for the spontaneous emission in Eq. (7). Without it, electron-hole recombination $|n,\vec{k}_\parallel\rangle\rightarrow|m,\vec{k}_\parallel\rangle$ with transition energy $\hbar\omega_{nm}(\vec{k}_\parallel)$ will lead to emission of radiation with angular frequency ω, which is in resonance with the Bohr frequency of the transition $\omega=\omega_{nm}(\vec{k}_\parallel)$. On the other hand the presence of the broadening function $U(\hbar\omega,\hbar\omega_{nm}(\vec{k}_\parallel);\Gamma_I,\Gamma_H)$ introduces a finite probability for the energy $\hbar\omega_{nm}(\vec{k}_\parallel)$, released in the $|n,\vec{k}_\parallel\rangle\rightarrow|m,\vec{k}_\parallel\rangle$ transition, to be emitted as radiation with angular frequency $\omega\neq\omega_{nm}(\vec{k}_\parallel)$, thus effectively describing nonresonant emission processes. The principle of conservation of energy then requires the probability for resonant emission in which $\omega=\omega_{nm}(\vec{k}_\parallel)$ to be reduced appropriately. The effect on the spectral emittance line shape is twofold. First the value $I(\hbar\omega)$ of the emittance at energy $\hbar\omega_{nm}(\vec{k}_\parallel)$ will be smaller for higher values of the broadening parameters Γ_I and Γ_H. Second for higher values of the broadening parameters Γ_I and Γ_H the increased probability for off-resonance emission leads to increase in the value of the spectral emittance $I(\hbar\omega)$ for energies in the neighborhood of the energy of the transition $\hbar\omega_{nm}(\vec{k}_\parallel)$. The combination of these two effects forms the mechanism behind the smearing of the sharp peaks in the emission spectrum associated with threshold energies $E_{nm}(0)$ for transitions between the electron and hole subbands $n\rightarrow m$. This mechanism of course is not restricted only to the CB1-HH2 transition in QW1 but is general. It can be used to explain the smearing of, or lack of, sharp features in the emission spectrum for different quantum wells and all types of transitions. In particular we attribute the lack of sharp features in the measured electroluminescence spectrum of QW2 presented in Fig. 4 to the above described mechanism and not due to the lack of forbidden transitions.

These conclusions are supported by our estimates of the broadening parameters Γ_I and Γ_H presented in Table I, which we have obtained by the method of line-shape fitting.[37] The inhomogeneous broadening parameter Γ_I attracts particular attention. Its values for QW1 and QW2 are similar (4 and 5.7 meV, respectively), while its value for QW3 (0.35 meV) is an order of magnitude smaller than those of QW1 and QW2. This is in qualitative agreement with the rapid nonlinear decrease in inhomogeneous broadening with well width examined in Ref 52. Inspection of the spontaneous emission spectrum of QW3, shown in Fig. 5, shows the presence of many well-resolved peaks, which, together with the data in Figs. 3 and 4, is consistent with the mechanism described in the previous paragraph. As mentioned in Sec. II the main physical factor behind the inhomogeneous broadening in this case is probably width fluctuations along a particular well. This implies that well width fluctuations play stronger role for QW1 and QW2, and for these two cases the inhomogeneous dominates over homogeneous broadening. For the widest well (QW3) the two types of broadening are of comparable magnitude. We have illustrated the effect of the homogeneous and inhomogeneous broadenings on the simulated spectrum for QW1 in Figs. 6(a) and 6(b), respectively. An increase in the two types of broadening decreases the peak height in accordance with the described mechanism and broadens the emittance lineshape. As an implication of the above discussion we predict that well-resolved peaks in the electroluminescence spectrum from QW heterostructures corresponding to transitions satisfying the conditions $n+m$ =even or forbidden transitions should be observable for small-enough values of the broadening parameters Γ_I and Γ_H. In practice this requires quantum wells of very good quality to reduce the well width fluctuations, and the associated phenomenological parameter Γ_I, as the measured signal is more sensitive to changes in the value of the inhomogeneous broadening.

E. QW2 (40 nm)

In Fig. 4(a) the measured and calculated spectra, using the parameters in Table I, are plotted for QW2. There is good overall agreement between the two curves especially regarding the onset. Note that we have used a single broadening parameter to achieve the best overall fit between the total measured spectra and the total simulated spectra. This has a

tendency to lead to an overestimation of the amount of broadening and consequently smooth out the simulated spectra to some degree. Future work will examine the importance of different amounts of broadening for each transition, which could lead to more precise reproduction of the sharp features in the measured spectra. The slight difference in the peak position can be mainly attributed to underestimation of V_{net}, and the disagreement in the tail structure can be attributed to both the CO_2 absorption and the slight underestimation of T_e. These small discrepancies in the exact numerical estimation of the fit parameters could be due to the fact that the minimum of χ^2 is not exactly the global one but close to it, or due to the resolution in the fitting parameter values. However, these slight numerical differences do not affect the conclusions in any way.

The simulations performed for the contribution from the different subband transitions $n \rightarrow m$ are presented in Fig. 4(b). We have found that the main transitions that contribute to the electroluminescence spectrum are the transitions from CB1 to the first five hole subbands HH1-HH5 and from the second conduction subband (CB2) to the first three heavy-hole subbands HH1-HH3. Their contribution was calculated using the best-fit parameters from Table I and is shown in Fig. 4(b). Note that in this case there are no confined LH states within the quantum well due to the lifting of the light-heavy-hole degeneracy by the compressive strain. We have found that transitions from the conduction subbands CB1 and CB2 to more remote hole subbands also contribute to the high-energy (tail) part of the spectrum, but due to very low statistical occupation of these states according to the Fermi-Dirac function their separate effect is marginal [for clarity we have not plotted these in Fig. 4(b)]. The contribution of significantly more transitions to the spectrum of QW2 (which contains the 40-nm-wide well) is commensurate with the effects of size quantization discussed earlier. The onset of the emission is almost entirely due to three transitions: CB1-HH1, CB1-HH2, and CB1-HH3. The slight shoulder near the CB1-HH2 marker is probably due to the CB1-HH2 transition, although, due to the combined statistical and broadening effects, the transitions CB1-HH1 and CB1-HH3 also contribute at this emission energy. The small shoulder in the experimental spectrum near the marker CB2-HH2 in Fig. 4(a), which designates the threshold energy of the CB2-HH2 transition, is probably due to the CB2-HH2 transition. The better resolved shoulder before the dip in the experimental spectrum is probably predominantly due to the contribution from the CB2-HH3 transition. We attribute the main peak in the experimental spectrum to the CB2-HH1 transition. Background signal at this emission frequency is also provided by the CB1-HH3, CB1-HH4, and CB2-HH2 transitions, but as can be seen in Fig. 4(b) the strength of the signal from these transitions is around two times smaller than the CB2-HH1 transition. The CB2-HH1 transition has the highest overall contribution to the emission spectrum of QW2 compared with all the other interband transitions.

F. Matrix elements and selection rules

In QW2 therefore, more clearly than in the case of QW1, because of the larger number of transitions present we see that the notion of forbidden transitions cannot be used in the interpretation of an electroluminescence spectrum of a QW heterostructure. Even more strikingly a transition, which in a simplified model falls in the category of forbidden transitions, actually contributes the strongest signal and gives the main contribution to the best observable feature in the experimental spectrum—its main peak. In order to understand this behavior we have investigated the momentum matrix elements $\langle m\vec{k}_{\|}|\vec{p}|n\vec{k}_{\|}\rangle$, which determine the selection rules of the problem. For unpolarized emission only the modulus squared of the momentum matrix elements $|p_{nm}(\vec{k}_{\|})|^2 = |\langle m\vec{k}_{\|}|\vec{p}|n\vec{k}_{\|}\rangle|^2$ contributes to the emittance $I(\hbar\omega)$, so we will focus on them. We would like to stress that the $\vec{k}_{\|}$ dependence of the squared matrix elements $|p_{nm}(\vec{k}_{\|})|^2$ is important and needs to be taken into account even for qualitative explanation of the emission spectrum. Because of the $\vec{k}_{\|}$ dependence, discussing selection rules or comparing strengths of transitions without regard for the 2D wave vector $\vec{k}_{\|}$ is inaccurate. In order to examine these effects on the spontaneous emission spectrum we have performed two steps. First, in the axial approximation all quantities in Eq. (7) are independent of the direction of the 2D wave vector $\vec{k}_{\|}$. For this isotropic band structure we have used a set of standard mathematical tools to perform the summation over the directional dependence in the wave vector $\vec{k}_{\|}$

$$\sum_{\vec{k}_{\|}} \rightarrow \frac{L^2}{(2\pi)^2}\int_{\mathrm{2DFBZ}} dk_{\|}^2 \rightarrow \frac{L^2}{(2\pi)^2} 2\pi \int_0^{2\pi/a} dk_{\|} k_{\|}$$

$$\rightarrow \frac{2\pi}{L}\sum_{k_{\|}} g^{(\mathrm{2D})}(k_{\|}), \tag{8}$$

where a is the lattice constant of the direct lattice, L is the linear size of the sample in the x-y plane, $g^{(\mathrm{2D})}(k_{\|}) \equiv \Sigma_{\vec{k}}\delta(|\vec{k}|-k_{\|}) = \frac{L^2}{2\pi}k_{\|}$ is the density of states per unit modulus $k_{\|}$ of the 2D crystal wave vector $\vec{k}_{\|}$, and the summation over the 2D wave vector $\vec{k}$ takes all possible values within the two-dimensional first Brillouin zone (2DFBZ). The important quantity in the resulting summation over the magnitude of the wave vector $\vec{k}_{\|}$ is the product between the squared momentum matrix element and the density of states per unit $k_{\|}$: $g^{(\mathrm{2D})}(k_{\|})|p_{nm}(k_{\|})|^2$. All the optically relevant information about the electron $|n,\vec{k}_{\|}\rangle$ and hole $|m,\vec{k}_{\|}\rangle$ wave functions, with 2D crystal wave vector quantum numbers satisfying the condition $|\vec{k}_{\|}| = k_{\|}$, are contained in this product which determines the strength of the transitions. The second step was to relate the above product directly to the transition energies by $g^{(\mathrm{2D})}[k_{\|}(\hbar\omega_{nm})]|p_{nm}[k_{\|}(\hbar\omega_{nm})]|^2$ using the function $k_{\|}(\hbar\omega_{nm})$, which is the inverse of $\hbar\omega_{nm}(k_{\|}) = E_n(k_{\|}) - E_m(k_{\|})$. Figure 7 depicts the functions $g^{(\mathrm{2D})}[k_{\|}(\hbar\omega_{nm})]|p_{nm}[k_{\|}(\hbar\omega_{nm})]|^2$ for the subband transitions CB1-HH1:HH5 and CB2-HH1:HH5, as obtained from the simulations of QW2 for zero net bias and the net bias from the best-fit parameters in Table I.

The fact that the selection rules $n+m=$even do not hold within the eight-band EFA approach and do not offer realistic description of the physical processes even in the case of symmetric quantum wells ($V_{\mathrm{net}}=0$) is clearly demonstrated in

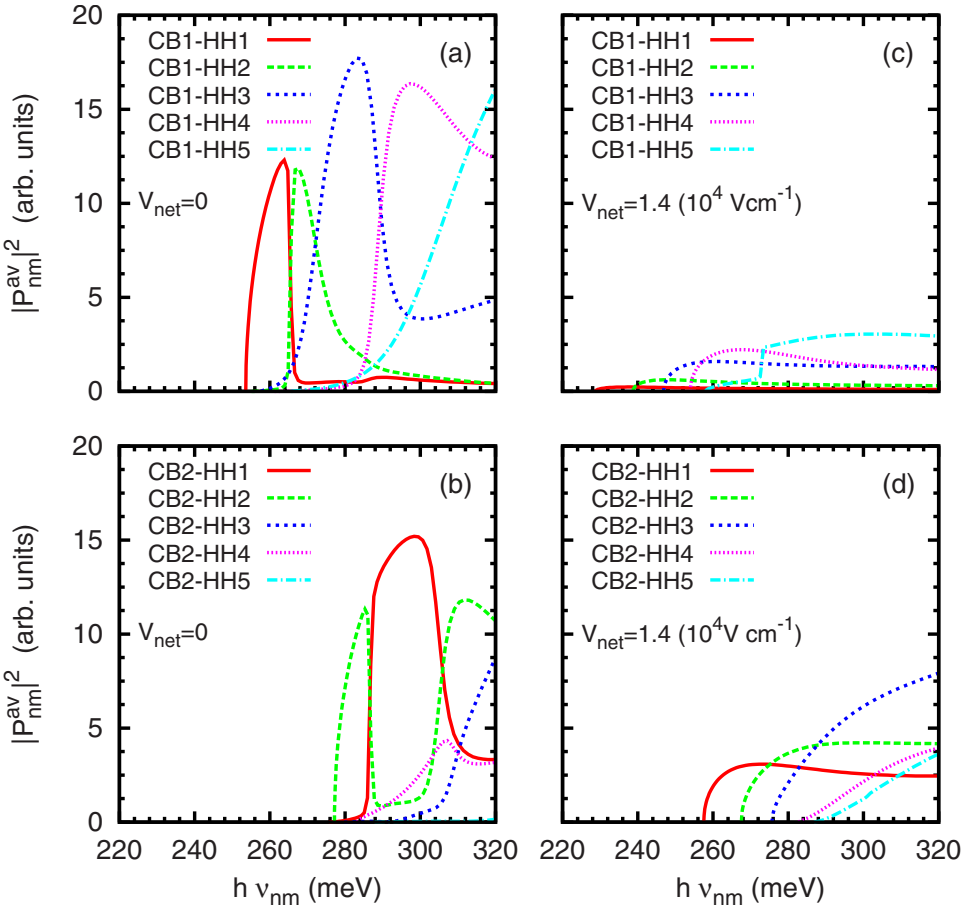

FIG. 7. (Color online) Momentum matrix elements as functions of transition energies obtained from the simulations for QW2 (40 nm wide) for zero net bias and finite net bias.

Figs. 7(a) and 7(b) by the fact that the product $g^{(2D)}(k_\parallel)|p_{nm}(k_\parallel)|^2$ is nonzero for all the depicted transitions. In addition we see that when we compare the strengths of different transitions we need to do so with regard to a particular transition energy $\hbar\omega_{mn}$. There are no strong or weak transitions, rather there are transitions that dominate over a part of the energy range. In particular, based on the information in Figs. 7(a) and 7(b), we would expect that the luminescence signal from QW2 under zero net bias would be dominated by the CB1-HH1 transition in the 252–265 meV range, CB1-HH2 in the 265–272 meV range, while beyond 272 meV the signal would be a mixture from several transitions.

The results for the dependence of the product $g^{(2D)}(k_\parallel)|p_{nm}(k_\parallel)|^2$ on the transition energies $\hbar\omega_{nm}$ for QW2, at the bias from the best-fit parameters in Table I, are presented in Figs. 7(c) and 7(d). The effect of the QCSE caused by the bias V_{net} manifests itself in the redshift of the onsets of the product $g^{(2D)}(k_\parallel)|p_{nm}(k_\parallel)|^2$ for all different transitions; for example, the onset of CB1-HH1 transition in Fig. 7(a) is at around 252 meV, while the onset of the same transition in Fig. 5(c) is at 228 meV. The effect that leads to qualitative difference is the change in the functions $g^{(2D)}[k_\parallel(\hbar\omega_{nm})]|p_{nm}[k_\parallel(\hbar\omega_{nm})]|^2$. For most of the transitions the peak value of the examined functions is lower for the finite bias case than for the zero bias. We attribute this to the overall decreased overlap of the electron and hole wave functions which tend to become localized in the opposite sides of the quantum well due to the SIA induced by the bias across the well. The major consequence of this effect on the luminescence properties would be the decrease in the value of the spectral emittance for increasing bias, if all the other factors were kept constant and were not influenced by the bias.

Another interesting trend that one can notice in Figs. 7(c) and 7(d) is that transitions from a particular conduction subband to lower heavy-hole subbands tend to have slightly higher values of the product $g^{(2D)}(k_\parallel)|p_{nm}(k_\parallel)|^2$ compared to transitions with smaller threshold energy. For example, in Fig. 7(c) the transition CB1-HH4 dominates over the transitions CB1-HH1:HH3, which have lower threshold energies, after some crossover energies specific to the transitions pair. This behavior can be explained qualitatively by the interplay of two effects. The first is the localization of the electron and hole wave functions on the opposite sides of a quantum well due to SIA induced by the net bias. The second is the fact that wave functions associated with higher eigenenergies tend to be less localized. As a consequence, in a biased quantum well the overlap between the electron and hole wave functions will increase with increased electron/hole energy, which will increase the momentum matrix element $|p_{nm}(k_\parallel)|^2$, and from there will tend to increase the product

$g^{(2D)}(k_\parallel)|p_{nm}(k_\parallel)|^2$. In the present model the increase in the electron/hole energy is equivalent to an increase in either the subband index n/m or the 2D crystal wave vector $\vec{k}_\parallel$, which can explain the observed trend. The same mechanism can explain why the product $g^{(2D)}(k_\parallel)|p_{nm}(k_\parallel)|^2$ is higher for the transitions from CB2 to the heavy-hole subbands compared with transitions from CB1 to the heavy-hole subbands. The above described mechanism is important for the understanding of the spectrum of QW2 in particular and to the electroluminescence spectra of QWs in general.

The data presented in Figs. 7(c) and 7(d) offer part of the explanation for the structure of the contribution of different subband transitions to the full luminescence signal. The other part of the explanation is statistical in nature—the electron and hole states occupational probabilities which in our model are described by the Fermi-Dirac function. A way to separate the two parts is to use the following gedanken—suppose that the electron and hole gases are degenerate with suitably chosen chemical potentials μ_e and μ_h such that $\mu_e - \mu_h = 276$ meV. Within this approximation inspection of Figs. 7(c) and 7(d) would imply that the dominant contribution to the spectrum is due to the CB2-HH1 transition with a significant contribution from CB1-HH3 and CB1-HH4, due to the mechanism qualitatively explained in the previous paragraph. The strengths of the CB1-HH1 and CB1-HH2 transitions are an order of magnitude smaller. On the other hand the data shown in Fig. 4(b) shows a much smaller difference between the peak heights of CB1-HH1, CB1-HH2, CB1-HH3, and CB2-HH1. To explain this we need to abandon the degenerate gas approximation and account for the statistical occupation of the electron/hole subband states. Comparison of the signal from CB1-HH1 with the CB1-HH2 transition in Fig. 4(b) shows that the statistical factor does not alter the relative contribution as implied within the degenerate gas approximation from the products $g^{(2D)}(k_\parallel)|p_{nm}(k_\parallel)|^2$ in Fig. 7(c). This can be attributed to the relatively small energy difference between HH1 and HH2 subbands. In contrast, despite the order-of-magnitude difference between the products $g^{(2D)}(k_\parallel)|p_{nm}(k_\parallel)|^2$ of the CB1-HH1 and CB2-HH1 transitions the peak height of their signal on Fig. 4(b) is of the same order of magnitude. The reason is the relatively big difference between the first and second conduction subbands as depicted in Fig. 2(e), as a result of which the relevant conduction-band states $|1,\vec{k}_\parallel\rangle$ have significantly higher occupational probability than their counterparts $|2,\vec{k}_\parallel\rangle$, thus compensating the order-of-magnitude difference between the $g^{(2D)}(k_\parallel)|p_{nm}(k_\parallel)|^2$ in this case. The same argument of combination of the band-structure effects with statistical factors can be used to explain the contribution of the other signals. The main conclusion of the above argument is that all the effects of the symmetry and overlap of electron and hole wave functions, including the selection rules if any, can be significantly modified by the occupational statistics, thus diminishing their significance for the analysis of the electroluminescence spectrum.

G. QW3 (100 nm QW)

The results from the line-shape fitting for QW3 are presented in Fig. 5(a) with the best-fit parameters given in Table I. (Note that in this case, we believe that some of the features in the measured spectra may be due to temperature fluctuations caused by the closed cycle helium cryostat used. In particular, the features observed in the measured spectra above 260 meV in QW3 are much less pronounced in measurements made at a different time on another LED, fabricated from the same wafer. However, it is very difficult experimentally to unambiguously confirm that the features above 260 meV in the data shown in Fig. 5 are solely due to temperature fluctuations. Further work is underway to investigate this.) The agreement between the measured spectrum (at 25 K) and the theoretical fit is satisfactory in the tail structure, indicating a good estimate of the effective temperature. There is good agreement between the three major peaks of the measured spectrum and theoretical calculations, including some shoulders in both the experimental and theoretical curves. The onset of the theoretical calculations shows small shoulders at energies close to the energies of the peaks at the onset of the experimental spectrum.

A possible explanation for the discrepancies between experimental measurements and theoretical simulations is the fact that we have performed the electronic structure calculations in the standard single-particle approximation instead of using some many-body scheme such as the Hartree-Fock approximation or the density functional theory (DFT). Many body effects might play more prominent roles in wider wells than in narrow ones. Another possible reason for the discrepancy is the band bending due to the modulation doping of the barrier materials which we have not taken into account. More extensive treatment of the problem including the above approximation is in advanced stage of development and will be reported elsewhere. Finally it is possible that the found minimum in χ^2 is not exactly the true global one but close to it. However these small discrepancies do not affect our conclusions.

The size quantization effects manifest themselves in the many possible transitions that contribute to the spectrum of QW3. We have found that more than 40 transitions contribute to the spectrum of QW3. The considerable number of transitions that contribute is a consequence of both the size quantization and the contribution from the so called forbidden transitions, confirming our conclusions from Secs. I–III. This, in combination with the low estimates for the homogeneous Γ_H and inhomogeneous Γ_I broadening parameters (presented in Table I), is consistent with the many observed sharp peaks in the experimental spectrum. The appreciable number of transitions contributing to the spontaneous emission spectrum of QW3 demonstrates the difficulties in the interpretation of luminescence experiments of wide quantum wells. Only ten transitions, assessed to be most relevant depending on their contribution to the full signal, have been shown in Fig. 5(b). We have found the CB1-HH8 transition to be the first significant contribution due to the very small value of the product $g^{(2D)}(k_\parallel)|p_{nm}(k_\parallel)|^2$ for the transitions CB1-HH1:HH7 which in this case cannot be compensated by the statistical factors as in QW2. This is the primary reason behind the absence of the three initial peaks, observed in the experimental curve, from the theoretical one. The transitions from higher lying conduction bands have more weight in the spectrum compared with QW2 and QW1.

V. CONCLUSIONS

We have investigated the low-temperature optical properties of InSb QW LEDs, with different barrier compositions, as a function of well width. Three devices were studied: QW1 had a 20 nm undoped InSb quantum well with a barrier composition of $Al_{0.143}In_{0.857}Sb$; QW2 had a 40 nm undoped InSb well with a barrier composition of $Al_{0.077}In_{0.923}Sb$; and QW3 had a 100 nm undoped InSb well with a barrier composition of $Al_{0.025}In_{0.975}Sb$. To identify the transitions that contribute to the measured spectra, the spectra have been simulated using an eight-band $\mathbf{k}.\mathbf{p}$ calculation of the band structure together with a first-order time-dependent perturbation method (Fermi golden rule) calculation of spectral emittance, taking into account broadening. In general there is good agreement between the measured and simulated spectra. Values of 4, 5.7, and 0.35 meV were obtained for the inhomogeneous broadening in QW1, QW2, and QW3, respectively, indicating the high material quality of the devices.

For QW1, the signature of two transitions (CB1-HH1, CB1-HH2) can be seen in the measured spectrum, whereas for QW2 and QW3 the signature of a large number (approximately 8 and 40, respectively) of transitions is present in the measured spectra. In particular, transitions to HH2 can be seen.

In QW2 we attribute the main peak in the experimental spectrum to the CB2-HH1 transition, which has highest overall contribution to the emission spectrum of compared with all the other interband transitions. This transition normally falls into the category of forbidden transitions, and in order to understand this behavior we have investigated the momentum matrix elements, which determine the selection rules of the problem. Further work is now underway to investigate the excitonic effects and also the effect of an external magnetic field on the spectral properties of these LEDs, which provide an exciting route to explore the unique properties of the InSb material system.

ACKNOWLEDGMENTS

QinetiQ acknowledges support for this work from the UK Department of Trade and Industry's Technology Programme. One of the authors (G.R.N.) acknowledges the support of The Royal Society.

*Present address: Department of Physics of Complex Systems, Eötvös Loránd University, H-1518 Budapest, Hungary.
†Corresponding author; grnash@qinetiq.com

[1] T. Ashley, L. Buckle, S. Datta, M. T. Emeny, D. G. Hayes, K. P. Hilton, R. Jefferies, T. Martin, T. J. Phillips, D. J. Wallis, P. J. Wilding, and R. Chau, Electron. Lett. **43**, 777 (2007).
[2] See, for example, A. D. Andreev, E. P. O'Reilly, A. R. Adams, and T. Ashley, Appl. Phys. Lett. **78**, 2640 (2001); E. A. Pease, L. R. Dawson, L. G. Vaughn, P. Rotella, and L. F. Lester, J. Appl. Phys. **93**, 3177 (2003); G. R. Nash, S. J. Smith, S. D. Coomber, S. Przeslak, A. Andreev, P. Carrington, M. Yin, A. Krier, L. Buckle, M. T. Emeny, and T. Ashley, Appl. Phys. Lett. **91**, 131118 (2007).
[3] N. Goel, J. Graham, J. C. Keay, K. Suzuki, S. Miyashita, M. B. Santos, and Y. Hirayama, Physica E (Amsterdam) **26**, 455 (2005).
[4] J. M. S. Orr, P. D. Buckle, M. Fearn, C. J. Storey, L. Buckle, and T. Ashley, New J. Phys. **9**, 261 (2007).
[5] See, for example, G. A. Khodaparast, R. E. Doezema, S. J. Chung, K. J. Goldammer, and M. B. Santos, Phys. Rev. B **70**, 155322 (2004); K. L. Litvinenko, B. N. Murdin, J. Allam, C. R. Pidgeon, M. Bird, K. Morris, W. Branford, S. K. Clowes, L. F. Cohen, T. Ashley, and L. Buckle, New J. Phys. **8**, 49 (2006); G. R. Nash, S. J. Smith, C. J. Bartlett, M. K. Haigh, N. T. Gordon, H. R. Hardaway, J. Edwards, L. Buckle, M. T. Emeny, and T. Ashley, IOP Conf. Proc. No. 187 (Institute of Physics, London, 2006), p. 437.
[6] M. K. Saker, D. M. Whittaker, M. S. Skolnick, C. F. McConville, C. R. Whitehouse, S. J. Barnett, A. D. Pitt, A. G. Cullis, and G. M. Williams, Appl. Phys. Lett. **65**, 1118 (1994).
[7] N. Dai, F. Brown, P. Barsic, G. A. Khodaparast, R. E. Doezema, M. B. Johnson, S. J. Chung, K. J. Goldammer, and M. B. Santos, Appl. Phys. Lett. **73**, 1101 (1998).
[8] N. Dai, F. Brown, R. E. Doezema, S. J. Chung, and M. B. Santos, Phys. Rev. B **63**, 115321 (2001).
[9] T. Kasturiarachchi, F. Brown, N. Dai, G. A. Khodaparast, R. E. Doezema, N. Goel, S. J. Chung, and M. B. Santos, J. Vac. Sci. Technol. B **24**, 2429 (2006).
[10] X. H. Zhang, R. E. Doezema, N. Goel, S. J. Chung, M. B. Santos, N. Dai, F. H. Zhao, and Z. S. Shi, Appl. Phys. Lett. **89**, 021907 (2006).
[11] S. J. Smith, G. R. Nash, M. Fearn, L. Buckle, M. T. Emeny, and T. Ashley, Appl. Phys. Lett. **88**, 081909 (2006).
[12] S. J. Smith, G. R. Nash, C. J. Bartlett, L. Buckle, M. T. Emeny, and T. Ashley, Appl. Phys. Lett. **89**, 111118 (2006).
[13] G. R. Nash, M. K. Haigh, H. R. Hardaway, L. Buckle, A. D. Andreev, N. T. Gordon, S. J. Smith, M. T. Emeny, and T. Ashley, Appl. Phys. Lett. **88**, 051107 (2006).
[14] I. Vurgaftman, J. R. Meyer, and L. R. Ram-Mohan, J. Appl. Phys. **89**, 5815 (2001).
[15] E. O. Kane, in *Semiconductors and Semimetals*, edited by R. K. Willardson and A. C. Beer (Academic, New York, 1966), Vol. 1, p. 75.
[16] R. Winkler, *Spin-Orbit Coupling Effects in Two-Dimensional Electron and Hole Systems* (Springer, Berlin, 2003).
[17] G. Bastard, Phys. Rev. B **24**, 5693 (1981).
[18] G. Bastard, Phys. Rev. B **25**, 7584 (1982).
[19] S. R. White and L. J. Sham, Phys. Rev. Lett. **47**, 879 (1981).
[20] M. Altarelli, U. Ekenberg, and A. Fasolino, Phys. Rev. B **32**, 5138 (1985).
[21] M. Altarelli, J. Lumin. **30**, 472 (1985).
[22] J. M. Berroir, Y. Guldner, J. P. Vieren, M. Voos, and J. P. Faurie, Phys. Rev. B **34**, 891 (1986).
[23] M. H. Weiler, in *Semiconductors and Semimetals*, edited by R. K. Willardson and A. C. Beer (Academic, New York, 1981), Vol. 16, p. 119.

[24] L. R. Ram-Mohan, K. H. Yoo, and R. L. Aggarwal, Phys. Rev. B **38**, 6151 (1988).
[25] J. M. Luttinger and W. Kohn, Phys. Rev. **97**, 869 (1955).
[26] J. M. Luttinger, Phys. Rev. **102**, 1030 (1956).
[27] C. R. Pidgeon and R. N. Brown, Phys. Rev. **146**, 575 (1966).
[28] D. Auvergne, J. Camassel, H. Mathieu, and A. Joulie, J. Phys. Chem. Solids **35**, 133 (1974).
[29] M. P. C. M. Krijn, Semicond. Sci. Technol. **6**, 27 (1991).
[30] D. Zhou and B. F. Usher, J. Phys. D **34**, 1461 (2001).
[31] T. Kasturiarachchi, F. Brown, N. Dai, G. A. Khodaparast, R. E. Doezema, S. J. Chung, and M. B. Santos, Appl. Phys. Lett. **88**, 171901 (2006).
[32] J. Singh, *Physics of Semiconductors and Their Heterostructures* (McGraw-Hill, New York, 1993).
[33] R. Loundon, *The Quantum Theory of Light* (Oxford University Press, New York, 2003).
[34] A. J. Wojtowicz, M. Kazmierczak, and A. Lempicki, J. Opt. Soc. Am. B **6**, 1106 (1989).
[35] A. Messiah, *Quantum Mechanics* (Dover, New York, 1999).
[36] G. Bastard, *Wave Mechanics Applied to Semiconductor Heterostructures* (EDP Sciences, France, 1992).
[37] G. Beadie, W. S. Rabinovich, D. S. Katzer, and M. Goldenberg, Phys. Rev. B **55**, 9731 (1997).
[38] A. Monakhov, A. Krier, and V. V. Sherstnev, Semicond. Sci. Technol. **19**, 480 (2004).
[39] M. Grupen and K. Hess, IEEE J. Quantum Electron. **34**, 120 (1998).
[40] J. F. Kielkopf, J. Opt. Soc. Am. **63**, 987 (1973).
[41] S. Kaushik and P. L. Hagelstein, IEEE J. Quantum Electron. **30**, 2547 (1994).
[42] W. H. Press, S. A. Teukolsky *et al.*, *Numerical Recipes* (Cambridge University Press, Cambridge, 2007).
[43] S. Kirkpatrick, C. D. Gelatt, and M. P. Vecchi, Science **220**, 671 (1983).
[44] K. V. Price, R. M. Storn, and J. A. Lampinen, *Differential Evolution: A Practical Approach to Global Optimization* (Springer, New York, 2005).
[45] K. F. Riley, M. P. Hobson, and S. J. Bence, *Mathematical Methods for Physics and Engineering* (Cambridge University Press, Cambridge, 2002).
[46] E. Rosencher and B. Vinter, *Optoelectronics* (Cambridge University Press, Cambridge, England, 2002).
[47] G. D. Sanders and Y. C. Chang, Phys. Rev. B **31**, 6892 (1985).
[48] G. D. Sanders and Yia-Chung Chang, Phys. Rev. B **32**, 5517 (1985).
[49] R. C. Miller, A. C. Gossard, and G. D. Sanders, Yia-Chung Chang, and J. N. Schulman, Phys. Rev. B **32**, 8452 (1985).
[50] A. Baldereschi and N. O. Lipari, Phys. Rev. B **3**, 439 (1971).
[51] X. H. Zhang, R. E. Doezema, N. Goel, S. J. Chung, M. B. Santos, N. Dai, F. H. Zhao, and Z. S. Shi, Appl. Phys. Lett. **89**, 021907 (2006).
[52] F. T. Vasko, P. Aceituno, and A. Hernández-Cabrera, Phys. Rev. B **66**, 125303 (2002).